MIT Open Access Articles

Novel Positively Charged Metal-Coordinated Nanofiltration Membrane for Lithium Recovery

Massachusetts Institute of Technology

DSpace@MIT

A novel positively-charged metal-coordinated nanofiltration membrane for lithium recovery

Li Wang[a,b], Danyal Rehman[c], Peng-Fei Sun[d], Akshay Deshmukh[c], Liyuan Zhang[b], Qi Han[a], Zhe Yang[b*], Zhongying Wang[a*], Hee-Deung Park[d], John H. Lienhard[c*] and Chuyang Y. Tang[b]

[a] School of Environmental Science and Engineering, Southern University of Science and Technology, Shenzhen 518055, China

[b] Department of Civil Engineering, the University of Hong Kong, Pokfulam, Hong Kong, SAR, P. R. China

[c] Department of Mechanical Engineering, Massachusetts Institute of Technology, Cambridge MA 02139, USA

[d] School of Civil, Environmental and Architectural Engineering, Korea University, Seoul, 02841, South Korea

[*] to whom correspondence should be addressed.

Zhongying Wang   e-mail: wangzy6@sustech.edu.cn;   tel.: +86-075588018040;

Zhe Yang   e-mail: zheyang@connect.hku.hk;   tel.: +852-2857 8470;

John H. Lienhard   e-mail: lienhard@mit.edu.;   tel.: +1-617-253-3790

Abstract

Nanofiltration (NF) if with high water flux and precise separation performance with high Li^+/Mg^{2+} selectivity, is ideal for lithium brine recovery. However, conventional polyamide-based commercial NF membranes are ineffective in lithium recovery processes due to their undesired Li^+/Mg^{2+} selectivity. In addition, they are constrained by the water permeance-selectivity trade-off, which means that highly permeable membrane often has lower selectivity. In this study, we developed a novel non-polyamide NF membrane based on metal coordinated structure, which exhibits simultaneously improved water permeance and Li^+/Mg^{2+} selectivity. Specifically, the optimized Cu-m-phenylenediamine (MPD) membrane demonstrated a high water permeance of 16.2 ± 2.7 LMH/bar and a high Li^+/Mg^{2+} selectivity of 8.0 ± 1.0, which surpassed the trade-off of permeance-selectivity. Meanwhile, the existence of copper in the Cu-MPD membrane further enhanced antibiofouling property and the metal-coordinated nanofiltration membrane possesses a pH-responsive protperty. Finally, a transport model based on the Nernst-Planck equations has been developed to fit the water flux and rejection of uncharged solutes to the experiments conducted. The model had a deviation below 2% for all experiments performed and suggested an average pore radius of 1.25 nm with a porosity of 0.21 for the Cu-MPD membrane. Overall, our study provides an exciting approach for fabricating non-polyamide high-performance nanofiltration membrane in the context of lithium recovery.

43 **TOC**

Metal-coordinated nanofiltration membrane

44
45
46
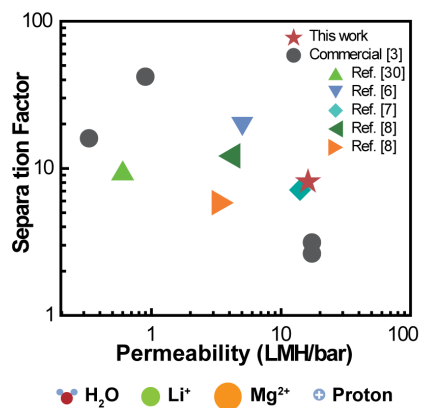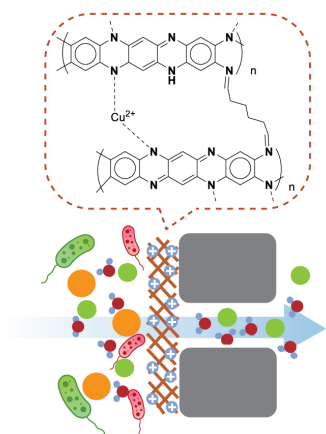
INTRODUCTION

Lithium, the lightest metal, has been extensively applied in rechargeable batteries with numerous important applications such as environmental-friendly vehicles, mobile communication equipment and other electric devices.[1] Lithium can be extracted from aqueous media including salt lakes, brines, and seawater, of which continental brine accounts for approximately ~ 59% of the worldwide lithium production.[2, 3] Therefore, many technologies have been developed to recover lithium from aqueous sources.[4-8] Compared to conventional approaches such as solar evaporation, chemical precipitation, adsorption, and solvent extraction, nanofiltration (NF) offers a promising alternative thanks to its simplicity, low energy consumption, and nontoxicity to the environment.[9-14]

NF is a pressure-driven membrane separation technology,[15] with a molecular weight cut-off (MWCO) ranging from 200 to 1000 Da. Commercial NF membranes adopt a thin-film composite (TFC) structure, where an ultra-thin polyamide rejection layer is formed on the microporous substrate with an interfacial polymerization reaction. The polyamide layer has a charged surface, ensuring an efficient separation of mono- and multi-valent ions at low operating pressures.[11, 16] Nanofiltration in lithium recovery is mainly employed as a pretreatment of the brine to eliminate the unwanted solutes (e.g., magnesium), with the following evaporation process to precipitate and crystallize lithium-related products.[3] Therefore, the high lithium selectivity is preferred to

68   improve the product purity. In addition, high permeance could further translate into

69   enhanced lithium production. Due to the low rejection of lithium ions by the Cu-MPD

70   membrane, there would not be significant lithium dilution to increase the energy

71   consumption in the process of precipitation. Furthermore, a highly-permeable

72   membrane could potentially reduce the energy consumption for the pretreatment by

73   lowering the operation pressure.[17] Consequently, NF has been extensively studied for

74   lithium recovery from brine.[18] Nevertheless, conventional polyamide-based NF

75   membranes are inefficient for achieving more precise membrane selectivity[19, 20] and

76   are adversely constrained by a trade-off between water permeance and selectivity, *i.e.,*

77   higher water permeance resulting in lower selectivity and vice versa.[10, 21-26]

78

79   Given the fact that the permselectivity limits of the polyamide chemistry, exploring

80   non-polyamide materials is critical to overcoming the longstanding tradeoff between

81   water permeance and selectivity.[10, 24, 25, 27, 28] MPD, as one of the crucial monomer (to

82   react with trimesoyl chloride) in fabricating fully-aromatic polyamide RO membrane,

83   has been dominating the RO market since its discovery. Unfortunately, the

84   fully-aromatic RO membrane has relatively low water permeance of 1-3 LMH/bar[10]

85   and RO membranes are also not efficient in Li/Mg selective separation due to the

86   negatively charged membrane surface.[3] For instance, Uyuni salar brine contains 15-18

87   g/L Mg and 0.7-0.9 g/L Li,[29] where Mg can interfere the lithium recovery process by

88   competing with Li in the formation of carbonate precipitate. It is difficult for

89   commercial membrane to selectively remove Mg^{2+} from the brine mixture due to their

90   comparable hydrated radius (Mg of 0.428 nm vs. Li of 0.382 nm).[13] Therefore, we

91   envisage an NF membrane fabricated by the self-polymerization of MPD assisted by

92   Cu^{2+}. Cu^{2+} promots the polymerization and crosslinking and also serves as the

93   positive-charge-center in the NF membrane. Moreover, this fabricating scheme of

94   Cu-MPD membrane can be readily integrated with the existing production line of

95   commercial TFC membrane.

96

97   In this study, we fabricated a non-polyamide NF membrane featuring a

98   positively-charged rejection layer consisting of Cu-MPD complexes. The Cu-MPD

99   complexes imparts the membrane with concurrently high water permeance and

100   enhanced the Mg^{2+}/Li^{+} selectivity. Meanwhile, the pH-responsive nature of the

101   Cu-MPD membrane enables further tuning of water permeance and rejection,

102   showing great potential in lithium recovery application. The fabricated membrane

103   successfully exceeded the state-of-art upper bound pertaining lithium recovery. Our

104   work shall have some insights into future membrane designs in the context of lithium

105   recovery.

106

107   **MATERIALS AND METHODS**

108   **Materials and Chemicals**

109   Deionized (DI) water was produced by Millipore system (Millipore, Billerica, MA)

110   and used for the preparation of all solutions. Polyethersulfone (PES) ultrafiltration

111   substrate (UH050, MWCO 50 kDa) was purchased from Microdyn Nadir.

112   *m*-phenylenediamine (MPD, flakes, 99%, Sigma-Aldrich), $CuCl_2 \cdot 2H_2O$ (Macklin,

113   China), $NaIO_4$ (99.5%, Macklin, China) and glutaraldehyde (GA, 50% in water,

114   Aladdin China) were used for fabricating membrane rejection layer. LiCl (anhydrous,

115   98%) and $MgCl_2 \cdot 6H_2O$ (98%) was purchased from Tokyo Chemical Industry (TCI,

116   Japan) and Uni-Chem, respectively. D-(+) Glucose (Mw. 180.16, Diekmann), D-(+)

117   sucrose (Mw. 342.3, Diekmann) and dextran (Mw 1000 and 2000, D-chem) were used

118   for the evaluation of membrane pore size. Absolute ethanol (≥99.8%) was purchased

119   from NORMAPUR VWR, Dorset, U.K. All chemicals are analytical grade unless

120   noted otherwise.

121

122   **Fabrication of Cu-MPD NF membrane**

123   As shown in Figure 1a, the fabrication protocol of the Cu-MPD NF membrane is

124   illustrated as follows: a piece of PES substrate (20 × 12 cm) was rinsed with DI water

125   and mounted into a home-made shaking reactor. First, a certain concentration of MPD

126   solution was added into the reactor with continuous shaking for 2 min to wet the

127   substrate surface. Then, $CuCl_2$ solution (1 wt% in DI water) was introduced into the

128   MPD solution to form the Cu-MPD complexes for 2 min. To accelerate the

129   polymerization, $NaIO_4$ solution (4 wt% in DI water) was then added into the mixture

130   and shaken for 5 h at 100 rpm. The membrane was taken out and immersed in DI

131   water overnight to remove the excessive chemicals. Afterwards, the membrane was

132 crosslinked in GA solution (2 wt% in ethanol solution) at 50 °C for 20 min.[30, 31]

133 Subsequently, the membrane was taken out from the GA ethanol solution and put in

134 an oven of 50 °C for another 20 min for post-treatment.[30] The resultant NF membrane

135 is denoted as CuX-MPD-NF, where X represents the mass ratio of Cu to MPD varied

136 from 0, 1/3, 1/2, 1 and 2.

137

138 **Membrane Characterization**

139 Surface morphologies of the Cu-MPD NF membrane and PES substrate were

140 examined by field emission scanning electron microscopy (FE-SEM, S-4800, Hitachi)

141 at 5 kV. Transmission electron microscopy (TEM, Philips CM100, 100 kV) was

142 utilized to obtain cross-sectional images of the surface layer of the resultant

143 membrane. Prior to characterization, membrane samples were embedded in a resin

144 (Epon, Ted Pella, CA), which was subsequently cut by an Ultracut E ultramicrotome

145 (Reichert, Inc. Depew, NY) into slices with a thickness of around 100 nm. These

146 slices then were placed on a copper grid and characterized in TEM. Atomic force

147 microscopy (AFM, Veeco, Nanoscope IIIa Multimode) was used to evaluate

148 membrane surface morphology and roughness. X-ray photoelectron spectroscopy

149 (XPS, Leybold Sengyang, China) was ultilized to analyze the surface chemical

150 compositions of the membranes. Water Contact angle (Attension Theta, Biolin

151 Scientific Sweden) was employed to measure the water contact angle of the prepared

152 membranes. The streaming potential (SurPASS 3 Electrokinetic Analyzer, Anton

153 PaarGmbH, Austria) was used for testing membrane surface charge. A quartz crystal

154 microbalance with dissipation (QCM-D, E4, QSense Biolin Scientific, Sweden) was

155 applied to examine the structure and mass change of the MPD-Cu complexes.[32]

156 Considering the limitation of QCM-D technique, the step of GA crosslinking was

157 omitted in the preparation of Cu-MPD complexes on the gold sensor. However, the

158 QCM-D measurements adopted the polymerization reaction between Cu^{2+} and MPD,

159 which allows us to reveal the important role of solution pH on affecting the structure

160 and water adsorption properties of Cu-MPD complexes. Therefore, the detailed

161 preparation procedures are described as follows: First, Cu1/2-MPD complex was

162 synthesized by the reaction 40 mL 2% MPD, 40 mL 2% CuCl$_2$ and 20 mL 4% NaIO$_4$,

163 with a polymerization time of 5 hr. The complex solution was further diluted 1000

164 times, and 100 uL of the diluted solution was added onto a gold-coated quartz wafer.

165 Please note that no GA was added for cross-linking due to the limitation of gold

166 sensor. Afterwards, the coated wafer was placed in oven at 60°C overnight for drying.

167 Furthermore, three of the coated wafers were placed in three parallel flow cells in the

168 QCM-D chamber. To initiate the test, pure water was infiltrated into the QCM-D flow

169 cells for 10 min to rinse and stabilize the system and then brines of pH 3, 7, 9 with a

170 concentration of 2000 ppm (MgCl$_2$ and LiCl mixture) were pumped into cells to

171 investigate the pH responsive behavior of the complex (Figure 4a). The frequency and

172 dissipation variation of the three wafers were recorded.

173

174 We further employed QCM-D open cell to investigate of the mechanism of the

175 membrane formation (Figure S6b). First, 200 μL of certain concentration of MPD

176 solution diluted by 10 times was added into the cell and stabilized for a period of time,

177 and then 200 μL of 0.2% CuCl$_2$ was added into it and wait until the frequency of the

178 system stabilized. Finally, 200 μL 0.4% NaIO$_4$ was rapidly added into the cell. The

179 system was further left for reaction until there was no change in the frequency was

180 observed. The frequency was recorded during the whole process and was converted

181 into the thickness of the developed membrane on the surface of the wafer through a

182 Sauerbrey equation.

183

184 The mechanism of QCM-D was described as follows: with a set of QCM-D

185 equipment, one can measure the frequency and dissipation value of the system. The

186 frequency variation can be further converted into mass change or thickness change of

187   the system by a Sauerbrey equation. On the other side, the dissipation value of the

188   coated materials can further translate into the structural change of the membrane.[33]

189

190   **Separation Performance Testing**

191   A cross-flow filtration setup was used to test the separation performance of the

192   membranes. Water permeance and rejection were measured at 5 bar at room

193   temperature, and each membrane was pre-pressured at 6 bar for 2 h to reach the

194   steady-state. Water flux can be calculated according to Eq. (1),

195    $$J_w = \frac{\Delta V}{\Delta t \times A} \tag{1}$$

196   where J_w (L m^{-2} h^{-1}) is the pure water flux; ΔV (L) is the volume of permeate; A (m^2)

197   is the active membrane area and Δt (h) is the sampling time.

198

199   For the rejection measurement, 1000 ppm MgCl$_2$ was used as feed solution. A

200   conductivity meter was used to measure the conductivity of permeate and feed to

201   determine the salt concentrations and then rejection defined by Eq. (2),

202    $$\mathrm{Rej}_i = 1 - \frac{c_p}{c_f} \tag{2}$$

203   where R is the salt rejection, while C_p and C_f are the salt concentrations of the

204   permeate and feed solution, respectively.

205

206   To examine the performance of the membranes in the application of Li recovery from

207   brine, a synthetic brine with a concentration of 2000 ppm (Mg/ Li mass ratio of 23)

208   was used as the feed solution and pH of the feed was adjusted from 3 to 9 using

10

209   diluted HCl and NaOH solutions.[34] Thus the separation factor $S_{Li,Mg}$ was calculated

210   by Eq. (3),

211   $$S_{Li,Mg} = \frac{C_{Li,p}/C_{Mg,p}}{C_{Li,f}/C_{Mg,f}} \qquad (3)$$

212   where $S_{Li,Mg}$ is the separation factor of Li^+ over Mg^{2+}, $C_{Li,p}$ and $C_{Li,f}$ are the Li^+

213   concentration in permeate and feed, respectively, $C_{Mg,p}$ and $C_{Mg,f}$ are the Mg^{2+}

214   concentration in permeate and feed, respectively. Inductive coupled plasma optical

215   emission spectrometer (ICP-OES, Optima 8 × 00, PerkinElmer) was used to measure

216   the concentration of Li^+ and Mg^{2+} according to our previous work.[32]

217

218   **Nanofiltration model for uncharged solutes**

219   The Donnan-Steric Pore model (DSPM) was used to develop a framework to

220   characterize transport across the fabricated Cu-MPD nanofiltration membranes.[35-39]

221   The extended Nernst-Planck equation was applied to model transmembrane transport.

222   For uncharged solutes, the migration term is neglected and transport is governed by

223   convection and diffusion.[40] The resulting expressions are integrated across the

224   membrane yielding closed-form expressions for individual solute fluxes. Water

225   transport is calculated using the Hagen-Poiseuille equation for flow through a tortuous

226   cylindrical pore, in line with observed membrane morphologies. The water and solute

227   fluxes are decoupled and provided by Eq. (4) and Eq. (5), respectively: [37, 39, 41, 42]

228   $$J_v = \frac{\epsilon r_p^2 \Delta P}{8 \tau \eta L} \qquad (4)$$

229   $$N_i = \frac{H_{i,C} J_v c_{i,F}}{1 - (1 - H_{i,C}) \exp(-Pe_i)} \qquad (5)$$

230   In Eq. (4), J_v is the volumetric water flux, ϵ is the porosity, r_P is the effective pore

231   radius, τ is the tortuosity, and η is the dynamic viscosity. Across the membrane, ΔP is

232   the applied hydraulic pressure and L is the membrane thickness. A membrane

233   thickness of 0.5 μm was assumed in this work, based on the cross-sectional SEM

234   images of the Cu-MPD membrane active layer (Figure S1). In Eq. (5), N_i is the molar

235   flux of solute i, which is a function of its convective hindrance factor, $H_{i,C}$, Péclet

236   number, Pe_i, and feed concentration, $c_{i,F}$. The permeate concentration of each solute,

237    $c_{i,P}$, is given by molar solute flux divided by the the volumetric solvent flux.

238

239   The Péclet number captures the ratio of convective to diffusive hindrance factors

240   across the membrane and is defined in Eq. (6):

241
$$Pe_i = \frac{K_{i,c} J_v L}{K_{i,d} D_i} \tag{6}$$

242   where, $K_{i,d}$ is the diffusive hindrance coefficient and D_i is the diffusion coefficient of

243   the solute in the solvent. In high Péclet number regimes, convection dominates and

244   the solute flux is primarily governed by the convective hindrance factor, the water

245   flux, and the concentration of the permeate. Conversely, in low Péclet number

246   regimes, the solute rejection is diffusion limited and only depends on the solute flux

247   and permeate concentration.

248

249   Hindrance parameters are usually written as functions of the relative penetrant size,

250   λ_i, where λ_i is defined as the ratio of the solutes' Stokes-Einstein radii to the

251   membrane effective pore radius.[43, 44] In this work, the convective and diffusive

252   hindrance processes are assumed to exhibit activated-type or Arrhenius-like behavior

253   whereby $K_{i,c}$ and $K_{i,d}$ are exponential functions of the convective and diffusive

254   fitting parameters, $\alpha_{i,c}$ and $\alpha_{i,d}$, respectively.[19, 45-48] The mathematical expressions

255   for $K_{i,c}$ and $K_{i,d}$ are given by:

256
$$K_{i,c} = \exp(-\alpha_{i,c}\lambda_i) \tag{7}$$

257
$$K_{i,d} = \exp(-\alpha_{i,d}\lambda_i) \tag{8}$$

258   The semi-empirical parameters $\alpha_{i,c}$ and $\alpha_{i,d}$ in Eq.s (7) and (8) reflect the averaged,

259   temperature-normalized energy barrier associated with solute convection and

260   diffusion processes, respectively. These parameters were used along with the

261   membrane porosity and effective pore radius are determined by the regression of

262   experimental data to the model for uncharged solutes.

263

264   Rejection of each solute species $(1 - c_{i,P}/c_{i,F})$ is given by: [37, 39, 41]

265
$$\text{Rej}_i = 1 - \frac{H_{i,C}}{1-(1-H_{i,C})\exp(-\text{Pe}_i)} \tag{9}$$

266   where Rej_i is the rejection of solute species i. In addition to fitting the rejection of

267   each solute, the model was also fit to the water flux measurements conducted as

268   detailed in Section 2.4. A particle swarm algorithm implemented in Matlab

269   (Mathworks, Natick, MA) was used to minimize the normalized least squared residual

270   between the model and experiments for all uncharged solutes: glucose, sucrose,

271   dextran (1 kDa), and dextran (2 kDa). [37, 39, 41] The objective function and fitted design

272 variables are provided in Eq. (10).

$$\text{Obj} = \min_{\epsilon, r_P, \alpha_{i,c}, \alpha_{i,d}} \left\{ \sum_{k=1}^{n_f} \left(\frac{J_{v,k}^{\text{mod}} - J_{v,k}^{\text{exp}}}{J_{v,k}^{\text{exp}}} \right)^2 + \sum_{i=1}^{n_s} \left[\sum_{k=1}^{n_f} \left(\frac{\text{Rej}_{i,k}^{\text{mod}} - \text{Rej}_{i,k}^{\text{exp}}}{\text{Rej}_{i,k}^{\text{exp}}} \right)^2 \right] \right\} \quad (10)$$

274 where the superscripts mod and exp denote the model and experiments. n corresponds

275 to the number of data points collected, where the subscripts s and f denote the

276 experimental data points representing solute rejection and water flux, respectively.

277

278 **Anti-biofouling test**

279 *Pseudomonas aeruginosa* PA14 was used as the model gram-negative bacteria for all

280 anti-biofilm and anti-biofouling assays. Approximately 15 mL of tryptic soy broth

281 (TSB) (BD, NJ, USA) was inoculated with a single colony of *P. aeruginosa* and

282 cultured in a shaking incubator at 37 °C and 250 rpm overnight.[49] Cells were then

283 centrifuged at 4 °C and 8000 rpm for 10 min, washed and suspended with sterile PBS

284 for the following tests.

285

286 Anti-biofilm experiments were carried out using a rotating disk biofilm reactor (DK20,

287 Biosurface, Montana, USA) under medium shear conditions. Briefly, the membrane

288 coupons were taped on the rotating disk. The biofilm was firstly formed in batch

289 mode (no flow) for 24 h with 1 mL PA14 suspension (10^6 CFU/mL) and 250 mL TSB

290 solution (300 mg/L). After reaching steady-state growth, the reactor was operated for

291 an additional 24 h with a continuous flow of the TSB solution (30 mg/L, 8.5 mL/min).

292 During the whole biofilm formation, the membrane coupon surfaces were

293 continuously exposed with fluid shear from the rotation of the disk (200 rpm). At the

294 end, the membrane coupons were removed from the disk for confocal laser scanning

295 microscopy (CLSM) (LSM700, Carl Zeiss, Jena, Germany) observation and viable

296 cell enumeration. [50, 51]

297

298 In addition, the anti-biofouling tests were conducted using a cross-flow membrane

299 module. A 4 L synthetic wastewater was recirculated using a high-pressure pump

300 (Hydra-cell pump, Wanner Engineering, Minneapolis, MN) with a flow rate of 1

301 L/min and pressure of 5 bar. Following cleaning and stabilization, the biofouling

302 experiments were initiated by injecting bacterial suspension (10^7 CFU/mL) into the

303 feed tank. After anti-biofouling, the membranes were carefully removed from the

304 module for CLSM analysis.

305

RESULTS AND DISCUSSION

sMicroscopic analysis and surface properties of the membranes.

Figure 1 presents the proposed chemical structure of the MPD-Cu complexes.[52] Briefly, MPD was self-polymerized and initiated by Cu^{2+} and $NaIO_4$ to form Cu-MPD complexes, and GA was used to improve the crosslinking degree of the resulting membrane.[31, 53] Specifically, Cu^{2+} could promote this self-polymerization by coordinating with MPD monomers and mediating the transfer of electrons from MPD to $NaIO_4$.[52] In addition, Cu^{2+} serves as the positive-charge center in the resultant complexes. After MPD monomer is oxidized, it would turn into a cationic radical and cleave from the coordination. The generated radical would further attack a free MPD monomer to propagate the polymer chain. Simultaneously, another free MPD monomer would occupy the vacancy of the left radical and start cycle of oxidation and polymerization, resulting propagated polymer chain. To confirm the formation of the positively charged Cu-MPD complexes, zeta potential measurements of the plain PES and Cu-MPD membranes were performed. As shown in Figure S2, the PES substrate was negatively charged throughout the pH range between pH 3 to 9. In contrast, the Cu-MPD NF membrane exhibited increased positive-charge density in the pH range from 3 to 7.4 (the isoelectric point). The positive-charge property on the surface of the membrane can be potentially ascribed to the Cu-MPD complexes containing cationic copper and protonated amino groups at acidic to neutral conditions.

328
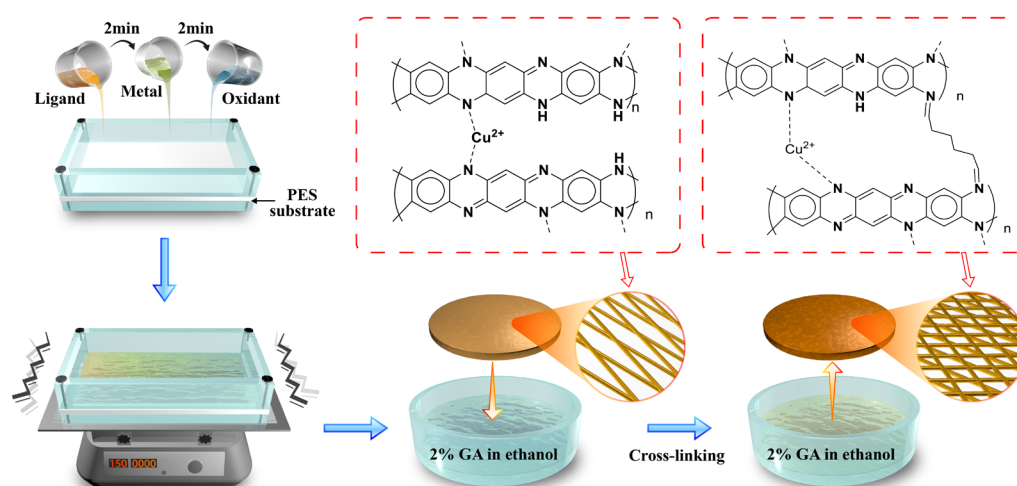
**Figure 1**. Membrane fabrication route and structural illustration of Cu-MPD NF membrane. MPD, $CuCl_2$ and $NaIO_4$ solution was poured onto the surface of the PES substrate, successively, followed by immersion of the surface-coated membrane into a GA/ethanol bath at 50 °C to form crosslinked Cu-MPD NF membrane.

333

To further confirm the formation of the Cu-MPD complexes, SEM and TEM techniques were applied to examine membrane surface and cross-section morphologies. As shown in Figure 2a, the pristine PES substrate had a flat surface (with root-mean-square roughness R_q of 12.2 nm in Figure 2e), with evenly distributed nanosized pores.[54] After coating the Cu-MPD complexes, the substrate pores vanished with numerous nodules prevailing on the surface of the Cu-MPD membrane (Figure 2c) with increased R_q of 22.1 nm in Figure 2f), which is in good agreement with the literature.[52] Cu-MPD membranes with different components (Table S1) and various Cu/MPD ratios were fabricated, and their morphologies and topographies were characterized through SEM (Figure S1a) and AFM (Figure S3). From there we can see that such nodules were absent when no Cu^{2+} or $NaIO_4$

345 involved in the coating process, confirming the indispensable roles of Cu^{2+} and $NaIO_4$

346 in promoting the formation of Cu-MPD complexes.[55]

347
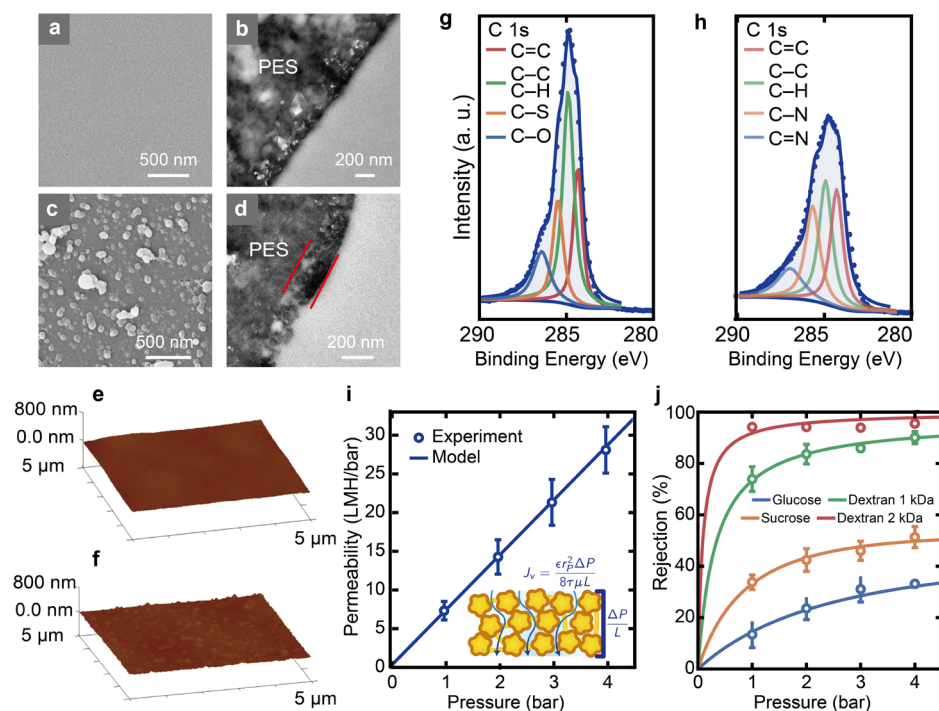
348
349 **Figure 2.** (a-b) SEM, (c-d) TEM, (e-f) AFM and (g-h) XPS of the prepared membrane;
350 (a, b, e, g) are for PES substrate, and (c, d, f, h) are for Cu1/2-MPD NF membrane. (i)
351 water flux against applied pressure; (j) rejection of neutral solutes under different
352 applied pressure for the Cu1/2-MPD membrane. For (i, j), dots are data obtained from
353 experimental work, and curves are model work.

354

355 TEM (Figure 2(b,d)) images present the cross-sections of the pristine PES substrate

356 and the Cu-MPD membrane. Compared to PES, the Cu-MPD membrane had a

357 thick-rejection layer of several hundred nanometers (marked between the two red

358 lines in Figure 2d). XPS was also used to confirm the formation of the Cu-MPD

359 membrane on the surface of the PES substrate (Figure 2(g,h) and Figure S4(a-c)).

360 Results in Figure 2(g,h) show the C 1s spectra of the PES substrate and the

361 Cu1/2-MPD membrane to reveal the chemical compositions of the synthesized

362 complex structure. Specifically, the deconvolution of C 1s spectrum of the PES

363 substrate (Figure 2g) showed four peaks at 284.4, 284.9, 285.3 and 286.1 eV,

364 attributed to the C=C, C-C, C-S and C-O of the backbone of the PES structure,

365 respectively.[56] In contrast, C-N and C=N were also detected in the Cu1/2-MPD

366 membrane at the bonding energy of 285.1 and 287.0 eV, respectively, in addition to

367 the peaks related with C=C and C-C of the polymerized MPD chain (Figure 2h).[53, 57]

368 N 1s spectrum was also investigated for the Cu1/2-MPD membrane to gain further

369 information of the membrane composition (Figure S4b). The peak at 399.4 eV

370 indicated the -NH, while the peak at 399.9 and 400.1 eV can be assigned to -N= and

371 -N-C, respectively. In addition, the signal of 401.1 eV indicates the presence of $-N^+=$,

372 which can be due to the coordination of Cu^{2+} and amino groups on the Cu-MPD

373 polymer chain.[53] The existence of Cu can also ben verified by the zeta potential

374 (Figure S4d) and isoelectric point data (Table S2), where the isoelectric point of

375 membrane Cu1/2-MPD was pH 7.4 ± 0.2 while for Cu0-MPD it was pH 5.3 ± 0.3.

376 Overall, the structural and compositional characterizations above demonstrate the

377 successful synthesis and loading of positively charged Cu-MPD onto a PES substrate.

378

379 To better understand the structure of the novel NF membrane, we use a DSPM-DE

380 model to characterize membrane porosity and pore radius. Figure 2i shows the

381 modeled and experimentally-measured water flux as a function of the applied

382   hydraulic pressure. A linear relationship is observed between water flux and hydraulic

383   pressure. The model, which is based on a Hagen-Poiseuille formulation, aligns very

384   strongly with the experiments. In Figure 2j, the rejection of each species is plotted as

385   a function of the applied hydraulic pressure. The DSPM-derived model is able to

386   capture the experimentally-observed variation of the solute rejection for all the solutes

387   tested across the range of hydraulic pressures analyzed. Solute rejection increases

388   with penetrant size in alignment with the physical intuition underlying size-based

389   selectivity. The rejection of each solute initially increases rapidly with transmembrane

390   pressure, before plateauing.[37, 39, 41] The increase in observed rejection is driven by an

391   increase in water flux, which leads to an increase in convective hindrance. As

392   transmembrane water flux continues to increase, solute rejection approachs the high

393   Péclet limit where $\text{Rej}_i \rightarrow 1 - H_{i,C}$. The fitted porosity and effective pore radius

394   obtained from the global optimization method were 0.21 and 1.25 nm, respectively.

395   Conventional nanofiltration membranes have porosities and effective pore radii that

396   range from 0.02-0.1 and 0.5-2 nm, respectively.[40, 58-62] The regressed parameters

397   suggest that the Cu-MPD membranes are significantly more porous than conventional

398   nanofiltration membranes, which aligns with observations from the SEM and TEM

399   images taken. The effective pore radius, however, is similar to current polyamide

400   membranes. The increased porosity with a comparable pore radius of synthesized

401   Cu-MPD membranes guarantees the excellent separation performance in a wide range

402   of NF-based applications beside the lithium recovery discussed below. Lastly, the

403   alignment between the model and experimental data highlights the model's predictive

404   capabilities in determining the rejection of uncharged solutes

405   coordination-complex-based membranes.

406

407   **Separation properties and lithium recovery performances of the membranes.**

408   Figure 3 presents the effect of Cu/MPD ratio on the separation performance of the

409   membranes. The actual copper loading concentration in membrane fabricated with

410   various Cu/MPD ratio was characterized with EDX (Figure S5) and ICP-OES (Table

411   S4).Without copper, the membrane exhibited relatively low rejection (22.6 ± 2.4%)

412   with low water permeance (1.3 ± 0.1 LMH/bar). With the increased Cu/MPD ratio, an

413   improved membrane water permeance and simultaneously enhanced $MgCl_2$ rejection

414   up to 90.0 ± 1.2% was observed. An optimized Cu/MPD ratio appears to be between

415   1/2 and 1, with the ratio of Cu/MPD strongly affecting the polymerization of Cu-MPD

416   complexes and therefore affecting their surface morphologies (Figure S1). We

417   speculate that the absence of copper led to the formation of incomplete and loose

418   MPD complex layer as Cu can promote the MPD self-polymerization.[52] Such a loose

419   structure could be further severely compacted at high transmembrane pressure,

420   leading to low water permeance and low $MgCl_2$ rejection. When Cu/MPD ratio

421   increased, the structure of the formed Cu-MPD complex became more rigid with

422   fewer defects, resulting in improved membrane separation performance. As the ratio

423   exceeded 1, however, synthesized Cu-MPD complex exhibited different assembly

424 pathways and decreased thickness as demonstrated by the different oligomer

425 absorption peaks in Figure S6a and QCM-D measurements in Figure S6b. This might

426 give some insight in explaining that the membrane exhibited an optimal structure with

427 Cu/MPD ratio varying 1/2 to 1. Separation performance of more membranes

428 fabricated with different components can be seen in Figure S7.

429

430 We further selected Cu1/2-MPD membrane as a benchmark to perform the lithium

431 recovery test from brine, and found its high Li^+/Mg^{2+} selectivity and high water

432 permeance (Figure 3(b,c)). Specifically, the pH of feed solution was varied from 3 to

433 9 to reveal the pH-dependent lithium recovery performance. Interestingly, unlike the

434 conventional polyamide-based NF membrane encountering the water

435 permeance-selectivity trade-off,[10] the Cu-MPD membrane demonstrated both high

436 water permeance of 16.2 ± 2.7 LMH/bar and high rejection against LiCl and $MgCl_2$ of

437 $32.3 \pm 7.6\%$ and $91.6 \pm 0.2\%$, respectively, at pH 3. The more pronounced

438 enhancement for rejecting divalent ions of $MgCl_2$ further led to a high Li^+/Mg^{2+}

439 selectivity value (8.0 ± 1.0, Figure 3b), which can be potentially due to the enhanced

440 Donnan exclusion effect, resulted from more protonated amino groups at lower pH

441 solution. At pH 9, in contrast, the membrane had systematically decreased water

442 permeance of 9.1 ± 0.7 LMH/bar and reduced rejection of LiCl and $MgCl_2$ of $21.7 \pm$

443 2.1% and $78.9 \pm 0.5\%$, respectively. Consequently, their Li^+/Mg^{2+} selectivity

444 decreased to 3.9 ± 0.1, potentially due to the neutralized membrane surface. As a

445   result, the high-performance Cu-MPD membrane at pH 3 showed relatively good

446   performance in the correlation in the upper bound diagram between membrane water

447   permeance and Li/Mg selectivity for the state-of-the-art NF membrane, including both

448   lab work and commercial membranes (Figure 3d and Table S3).[63] It is worthwhile to

449   note that different testing conditions (e.g., operating pressure, feed concentration,

450   temperature and etc.) could significantly affect membrane separation performance. In

451   order to exclude the effect of operation conditions, the correlation between water-salt

452   permselectivity A/B_{MgCl2} vs. membrane permeance A and salt-salt selectivity

453   B_{LiCl}/B_{MgCl2} vs. membrane permeance A to examine membrane intrinsic transport

454   properties were plotted in the revised Supporting Information (Figure S11).

455

456   The pH of the feed solution would greatly affect the charge density of the membrane

457   active layer by changing the protonation condition of the amino groups in the

458   Cu-MPD complex. Specifically, when pH increases, fewer amino groups are

459   protonated, leading to reduced positive charge density of membrane active layer; As a

460   result, the electrostatic repulsion between these amino group decreases, leading to a

461   tighter structure of the Cu-MPD complex. Therefore, the pore size of the membrane is

462   reduced, and vice versa. When pH decreased, more amino groups became protonated,

463   leading to higher positive charge-density. This electrostatic repulsion would result in a

464   looser structure of the Cu-MPD complex. Thus, more water could be captured and

465   enter the nano pores of the Cu-MPD complex.
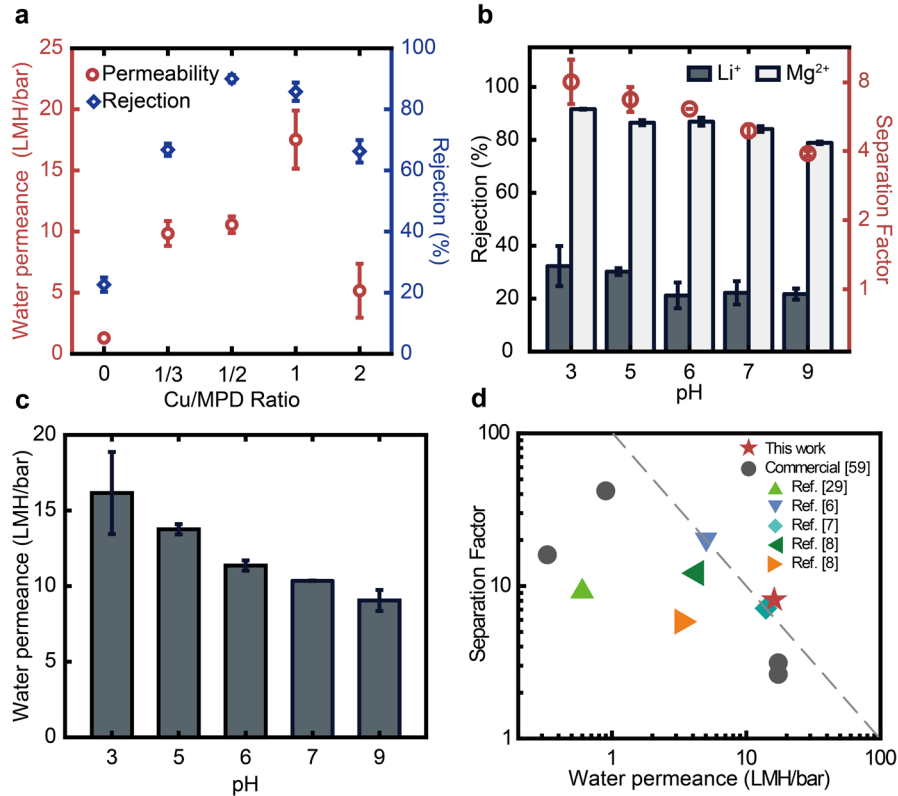
Figure 3. Separation properties and lithium recovery performances of the Cu-MPD membranes. (a) Water permeance and Mg^{2+} rejection of membrane fabricated at varied Cu/MPD ratios, (b) lithium recovery performance of Cu-MPD NF membrane as a function of pH. Membrane rejection of Li^+, Mg^{2+} and separation factor (S) of Li^+/Mg^{2+} and (c) pure water permeance in the pH range from 3-9 and (d) the performance boundary between water permeance and Li^+/Mg^{2+} separation factor, including literature results, commercial membranes and the membrane developed from this study. All filtration tests are operated at 5 bar, 1000 ppm of $MgCl_2$ was used for evaluating membrane rejection for Mg^{2+} and a synthetic brine of a concentration of 2000 ppm (Li/Mg mass ratio of 23) was used for evaluating membrane lithium recovery performance. All the presented results are based on three membrane coupons replicates.

Mechanisms of the pH-responsive properties of the membranes.

To gain a better understanding of the pH-responsive membrane properties, we further performed QCM-D analysis on the structure and mass change of the Cu-MPD membranes under different pH conditions. A significant decrease in frequency was observed when pH decreased from 9 to 3 shown in Figure 4a, implying an increased

485 mass of Cu-MPD membrane. Such an increase is caused by more-opening pore

486 structure that could accomodate more water molecules and ions. Indeed, the highest

487 Dissipation (D) value was obtained for the Cu-MPD complexes at pH 3, thanks to the

488 enhanced electrostatic repulsion for the protonated amino groups at a lower pH. The

489 looser structure further explains the enhanced water absorption (Figure 4a) as well as

490 the improved membrane water permeance (Figure 3b). On the contrary, a higher pH

491 resulted in both decreased changes in D and frequency (F) values, corresponding to a

492 more rigid layer structure and a lower water absorption, respectively. This can be

493 potentially due to the diminished charge interaction, which can be certified by the zeta

494 potential results shown in Figure S2.

495
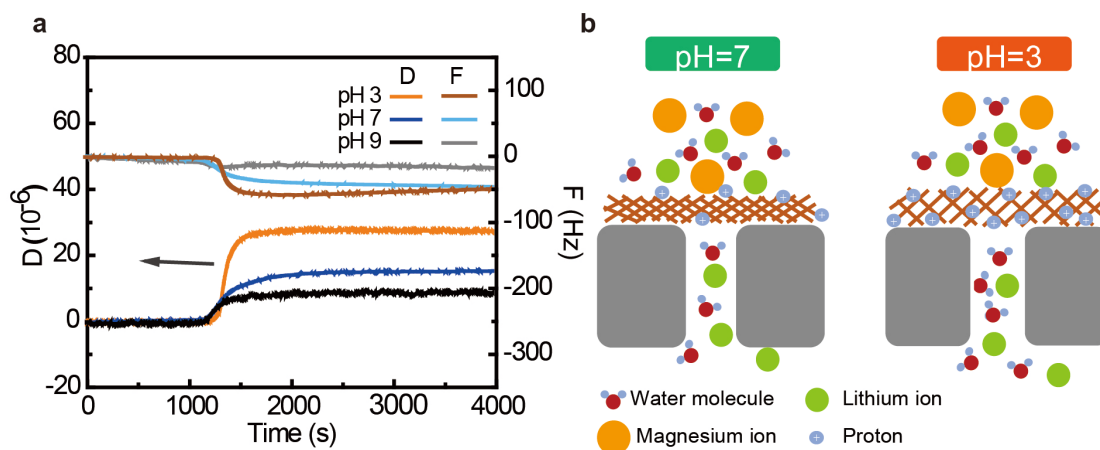
496

497 Figure 4. (a) QCM-D characterization of Cu-MPD NF membrane using simulated
498 brine of 2000 ppm at pH 3, 7 and 9. Cu/MPD complexes at ratio of 1/2 were coated
499 on the surface of the gold senor. To perform the charaterization, DI water was first
500 filtrated through the system for stabilizing. Subsequently, brine with different pH was
501 introduced with the real-time measured frequency and dissipation and (b) a schematic
502 illustration of a mechanism for pH-responsive membrane.

503

Antibiofouling properties of the membranes.

504

505 Conventional polyamide-based NF membranes are prone to biofouling and

506 significantly increase its operation costs.[32] Copper is a well-known antimicrobial

507 agent.[64, 65] In this regard, antibiofouling and antimicrobial properties of the Cu-MPD

508 membrane were investigated. The CLSM images (Figure 5b) show reduced biofilm

509 thickness after a 10 h filtration test for the copper-contained membrane compared to

510 the control counterpart. Moreover, compared to the control membrane showing

511 significant water flux loss, the Cu-MPD membrane exhibited only a slightly reduced

512 water flux thanks to the antifouling capability as a result of the loaded copper (Figure

513 5a). We further performed the significance test for the two groups of data of colony

514 forming unit (Supporting Information Figure S8), and the calculated P value is 0.03,

515 implying a significance of the antimicrobial ability between membrane with and

516 without copper. We also performed static antimicrobial tests using the rotating disc

517 reactor. After 40 h rotating disc experiment, the Cu-MPD membrane and control were

518 taken out from the reactor for CLSM imaging (Figure S9a), which showed that fewer

519 live bacteria can be observed on the surface of Cu-MPD membrane in line with the

520 anti-biofouling tests. In addition, more live bacteria were observed on the plate spread

521 with bacteria suspension solutions from control, compared to that of Cu-MPD

522 membrane (Figure S8(b,c)).

523
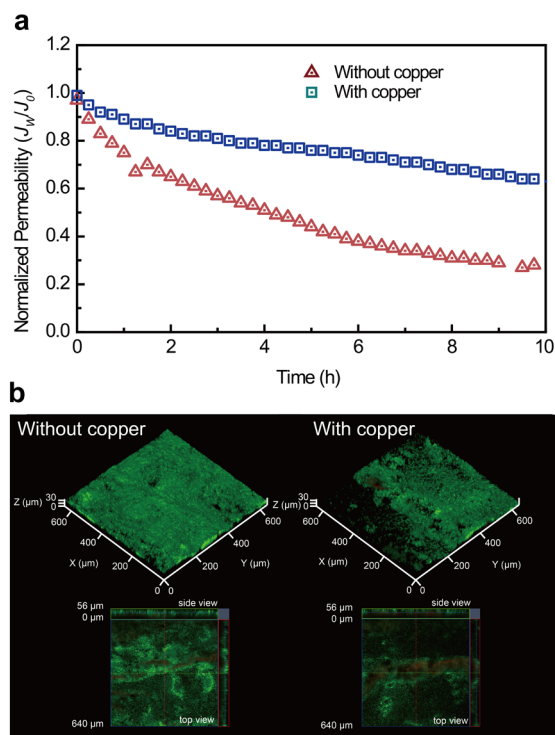
Figure 5. Anti-biofouling tests of the membranes with and without copper using a cross flow filtration system and rotating disc reactor. (a) normalized membrane water flux with and without copper, (b) CLSM image of the membrane surface with and without copper after 10 h filtration at 10 bar.

IMPLICATIONS

We developed a novel non-polyamide NF membrane with Cu^{2+} assisted MPD self-polymerization. The fabrication conditions and the effect of Cu^{2+} on membrane structure and separation performance were systematically investigated. The optimized membrane exhibited high water permeance and high Li^+/Mg^{2+} selectivity, which exceeded the upper bound of the lab-made membrane as well as commercial membranes. Furthermore, the membrane showed both increased water permeance and salt rejection at lower pH. The underlying mechanism in membrane structure and surface charge density at different pH was elucidated with the aid of QCM-D. An NF model was also developed in this work to fit water flux and rejection of uncharged

27

541   solutes to experimental data. The model was within a 2% deviation of all conducted

542   experiments. Lastly, the Cu-MPD NF membrane showed good anti-biofouling ability,

543   accounted for its Cu^{2+} loading and surface positive charge. The high porsity and

544   suitable pore radius implied by modelling and separation performance highlight the

545   great promise of Cu-MPD membranes in the fields relevant to NF applications.

546   Additionally, this method can be further extended by tuning pore size using different

547   monomers or cations for versatile applications, such as heavy metal removal and dye

548   retention.

549

550   **ASSOCIATED CONTENT**

551   The Supporting Information is available free of charge at DOI:

552   XXXXX

553

554   **AUTHOR INFORMATION**

555   **Corresponding Authors**

556   Zhongying Wang   e-mail: wangzy6@sustech.edu.cn;   tel.: +86-075588018040;

557   Zhe Yang   e-mail: zheyang@connect.hku.hk;   tel.: +852-2857 8470;

558   John H. Lienhard   e-mail: lienhard@mit.edu.;   tel.: +1-617-253-3790

559

560   **Authors**

561   **Li Wang:** 0000-0001-9829-4729

562   **Danyal Rehman:** 0000-0001-9457-191X

563   **Peng-Fei Sun:** 0000-0002-3942-9766

564   **Akshay Deshmukh:** 0000-0002-3693-1902

565   **Liyuan Zhang:** 0000-0002-7585-5607

566   **Qi Han:** 0000-0003-3493-0655

567   **Zhe Yang:** 0000-0003-0753-3902

568   **Zhongying Wang:** 0000-0002-7869-6859

569   **Hee-Deung Park:** 0000-0002-5769-335X

570   **John H. Lienhard:** 0000-0002-2901-0638

571   **Chuyang Y. Tang:** 0000-0002-7932-6462

572

573   **Notes**

574   The authors declare no competing financial interest.

575

583

References:

1. Goriparti, S.; Miele, E.; De Angelis, F.; Di Fabrizio, E.; Proietti Zaccaria, R.; Capiglia, C., Review on Recent Progress of Nanostructured Anode Materials for Li-Ion Batteries. *J. Power Sources* **2014,** *257*, 421-443.

2. Swain, B., Recovery and Recycling of Lithium: A Review. *Sep. Purif. Technol.* **2017,** *172*, 388-403.

3. Li, X.; Mo, Y.; Qing, W.; Shao, S.; Tang, C. Y.; Li, J., Membrane-Based Technologies for Lithium Recovery from Water Lithium Resources: A Review. *J. Membr. Sci.* **2019,** *591*, 117317

4. Zhao, X.; Yang, H.; Wang, Y.; Sha, Z., Review on the Electrochemical Extraction of Lithium from Seawater/brine. *J. Electroanal. Chem.* **2019,** *850*, 1572-6657.

5. Li, X.; Zhang, C.; Zhang, S.; Li, J.; He, B.; Cui, Z., Preparation and Characterization of Positively Charged Polyamide Composite Nanofiltration Hollow Fiber Membrane for Lithium and Magnesium Separation. *Desalination* **2015,** *369*, 26-36.

6. Xu, P.; Wang, W.; Qian, X.; Wang, H.; Guo, C.; Li, N.; Xu, Z.; Teng, K.; Wang, Z., Positive Charged PEI-TMC Composite Nanofiltration Membrane for Separation of Li^+ and Mg^{2+} from Brine with High Mg^{2+}/Li^+ Ratio. *Desalination* **2019,** *449*, 57-68.

7. Zhang, H.-Z.; Xu, Z.-L.; Ding, H.; Tang, Y.-J., Positively Charged Capillary Nanofiltration Membrane with High Rejection for Mg^{2+} and Ca^{2+} and Good Separation for Mg^{2+} and Li^+. *Desalination* **2017,** *420*, 158-166.

8. Guo, C. S.; Li, N.; Qian, X. M.; Shi, J.; Jing, M. L.; Teng, K. Y.; Xu, Z. W., Ultra-Thin Double Janus Nanofiltration Membrane for Separation of Li^+ and Mg^{2+}: "Drag" Effect from Carboxyl-containing Negative Interlayer. *Sep. Purif. Technol.* **2020,** *230*, 115567.

9. Quist-Jensen, C. A.; Ali, A.; Drioli, E.; Macedonio, F., Perspectives on Mining from Sea and Other Alternative Strategies for Minerals and Water Recovery-the Development of Novel Membrane Operations. *J. Taiwan Inst. Chem. Eng.* **2019,** *94*, 129-134.

10. Yang, Z.; Guo, H.; Tang, C. Y., The Upper Bound of Thin-Film Composite (TFC) Polyamide Membranes for Desalination. *J. Membr. Sci.* **2019,** *590*, 117297.

11. Zhang, Y.; Wang, L.; Sun, W.; Hu, Y.; Tang, H., Membrane Technologies for Li^+/Mg^{2+} Separation from Salt-Lake Brines and Seawater: A Comprehensive Review. *J. Ind. Eng. Chem.* **2020,** *81*, 7-23.

12. Ahdab, Y. D.; Rehman, D.; Lienhard, J. H., Brackish Water Desalination for Greenhouses: Improving Groundwater Quality for Irrigation Using Monovalent Selective Electrodialysis Reversal. *J. Membr. Sci.* **2020,** *610*, 118072.

13. Wen, X.; Ma, P.; Zhu, C.; He, Q.; Deng, X., Preliminary Study on Recovering Lithium Chloride from Lithium-Containing Waters by Nanofiltration. *Sep. Purif. Technol.* **2006,** *49*, (3), 230-236.

14. Ahdab, Y. D.; Rehman, D.; Schücking, G.; Barbosa, M.; Lienhard, J. H., Treating Irrigation Water Using High-Performance Membranes for Monovalent Selective

626   Electrodialysis. *ACS ES&T Water* **2020,** *1*, 117-124.

627   15. Guo, H.; Peng, L. E.; Yao, Z.; Yang, Z.; Ma, X.; Tang, C. Y., Non-Polyamide
628   Based Nanofiltration Membranes Using Green Metal-Organic Coordination
629   Complexes: Implications for the Removal of Trace Organic Contaminants. *Environ.*
630   *Sci. Technol.* **2019,** *53*, (5), 2688-2694.

631   16. Yang, Z.; Ma, X.-H.; Tang, C. Y., Recent Development of Novel Membranes for
632   Desalination. *Desalination* **2018,** *434*, 37-59.

633   17. Yang, Z.; Sun, P.-F.; Li, X.; Gan, B.; Wang, L.; Song, X.; Park, H.-D.; Tang, C. Y.,
634   A Critical Review on Thin-Film Nanocomposite Membranes with Interlayered
635   Structure: Mechanisms, Recent Developments, and Environmental Applications.
636   *Environ. Sci. Technol.* **2020,** *54*, (24), 15563-15583.

637   18. Somrani, A.; Hamzaoui, A. H.; Pontie, M., Study on Lithium Separation from
638   Salt Lake Brines by Nanofiltration (NF) and Low Pressure Reverse Osmosis (LPRO).
639   *Desalination* **2013,** *317*, 184-192.

640   19. Epsztein, R.; DuChanois, R. M.; Ritt, C. L.; Noy, A.; Elimelech, M., Towards
641   Single-Species Selectivity of Membranes with Subnanometre Pores. *Nature Nanotech.*
642   **2020,** *15*, (6), 426-436.

643   20. Sarkar, P.; Modak, S.; Karan, S., Ultraselective and Highly Permeable Polyamide
644   Nanofilms for Ionic and Molecular Nanofiltration. *Advanced Functional Materials*
645   **2021,** *31*, (3), 2007054.

646   21. Robeson, L. M., Correlation of Separation Factor versus Permeability for
647   Polymeric Membranes. *J. Membr. Sci.* **1991,** *62*, (2), 165-185.

648   22. Robeson, L. M., The Upper Bound Revisited. *J. Membr. Sci.* **2008,** *320*, (1-2),
649   390-400.

650   23. Geise, G. M.; Park, H. B.; Sagle, A. C.; Freeman, B. D.; McGrath, J. E., Water
651   Permeability and Water/Salt Selectivity Trade-Off in Polymers for Desalination. *J.*
652   *Membr. Sci.* **2011,** *369*, (1-2), 130-138.

653   24. Geise, G. M.; Paul, D. R.; Freeman, B. D., Fundamental Water and Salt Transport
654   Properties of Polymeric Materials. *Prog. Polym. Sci.* **2014,** *39*, (1), 1-42.

655   25. Werber, J. R.; Deshmukh, A.; Elimelech, M., The Critical Need for Increased
656   Selectivity, Not Increased Water Permeability, for Desalination Membranes. *Environ.*
657   *Sci. Technol. Lett.* **2016,** *3*, (4), 112-120.

658   26. Roy, Y.; Lienhard, J. H., A Framework to Analyze Sulfate versus Chloride
659   Selectivity in Nanofiltration. *Environ. Sci.: Water Res. Technol.* **2019,** *5*, (3), 585-598.

660   27. Park, H. B.; Kamcev, J.; Robeson, L. M.; Elimelech, M.; Freeman, B. D.,
661   Maximizing the Right Stuff: The Trade-Off between Membrane Permeability and
662   Selectivity. *Science* **2017,** *356*, (6343), 1137.

663   28. Werber, J. R.; Osuji, C. O.; Elimelech, M., Materials for Next-Generation
664   Desalination and Water Purification Membranes. *Nat. Rev. Mater.* **2016,** *1*, (5), 1-15.

665   29. Meshram, P.; Pandey, B. D.; Mankhand, T. R., Extraction of Lithium from
666   Primary and Secondary Sources by Pre-treatment, Leaching and Separation: A
667   Comprehensive Review. *Hydrometallurgy* **2014,** *150*, 192-208.

668 30. Lv, Y.; Du, Y.; Qiu, W. Z.; Xu, Z. K., Nanocomposite Membranes via the
669 Codeposition of Polydopamine/Polyethylenimine with Silica Nanoparticles for
670 Enhanced Mechanical Strength and High Water Permeability. *ACS Appl. Mater.*
671 *Interfaces* **2017**, *9*, (3), 2966-2972.

672 31. Lv, Y.; Yang, H.-C.; Liang, H.-Q.; Wan, L.-S.; Xu, Z.-K., Nanofiltration
673 Membranes via Co-deposition of Polydopamine/Polyethylenimine Followed by
674 Cross-linking. *J. Membr. Sci.* **2015**, *476*, 50-58.

675 32. Yang, Z.; Wu, Y.; Wang, J.; Cao, B.; Tang, C. Y., In Situ Reduction of Silver by
676 Polydopamine: A Novel Antimicrobial Modification of A Thin-Film Composite
677 Polyamide Membrane. *Environ. Sci. Technol.* **2016,** *50*, (17), 9543-50.

678 33. Guo, H.; Yao, Z.; Yang, Z.; Ma, X.; Wang, J.; Tang, C. Y., A One-Step Rapid
679 Assembly of Thin Film Coating using Green Coordination Complexes for Enhanced
680 Removal of Trace Organic Contaminants by Membranes. *Environ. Sci. Technol.* **2017,**
681 *51*, (21), 12638-12643.

682 34. Li, W.; Shi, C.; Zhou, A.; He, X.; Sun, Y.; Zhang, J., A Positively Charged
683 Composite Nanofiltration Membrane Modified by EDTA for $LiCl/MgCl_2$ Separation.
684 *Sep. Purif. Technol.* **2017,** *186*, 233-242.

685 35. Roy, Y.; Lienhard, J. H., Factors Contributing to the Change in Permeate Quality
686 upon Temperature Variation in Nanofiltration. *Desalination* **2019,** *455*, 58-70.

687 36. Roy, Y.; Warsinger, D. M.; Lienhard, J. H., Effect of Temperature on Ion
688 Transport in Nanofiltration Membranes: Diffusion, Convection and Electromigration.
689 *Desalination* **2017,** *420*, 241-257.

690 37. Labban, O.; Liu, C.; Chong, T. H.; Lienhard, J. H., Relating Transport Modeling
691 to Nanofiltration Membrane Fabrication: Navigating the Permeability-Selectivity
692 Trade-Off in Desalination Pretreatment. *J. Membr. Sci.* **2018,** *554*, 26-38.

693 38. Roy, Y.; Sharqawy, M. H.; Lienhard, J. H., Modeling of Flat-Sheet and
694 Spiral-Wound Nanofiltration Configurations and its Application in Seawater
695 Nanofiltration. *J. Membr. Sci.* **2015,** *493*, 360-372.

696 39. Labban, O.; Liu, C.; Chong, T. H.; Lienhard, J. H., Fundamentals of
697 Low-Pressure Nanofiltration: Membrane Characterization, Modeling, and
698 Understanding the Multi-Ionic Interactions in Water Softening. *J. Membr. Sci.* **2017,**
699 *521*, 18-32.

700 40. Ahmad, A.; Ooi, B.; Mohammad, A. W.; Choudhury, J., Composite Nanofiltration
701 Polyamide Membrane: A Study on the Diamine Ratio and Its Performance Evaluation.
702 *Ind. Eng. Chem. Res.* **2004,** *43*, (25), 8074-8082.

703 41. Geraldes, V.; Alves, A. M. B., Computer Program for Simulation of Mass
704 Transport in Nanofiltration Membranes. *J. Membr. Sci.* **2008,** *321*, (2), 172-182.

705 42. Bowen, W. R.; Welfoot, J. S., Modelling the Performance of Membrane
706 Nanofiltration-Critical Assessment and Model Development. *Chem. Eng. Sci.* **2002,**
707 *57*, (7), 1121-1137.

708 43. Dechadilok, P.; Deen, W. M., Hindrance Factors for Diffusion and Convection in
709 Pores. *Ind. Eng. Chem. Res.* **2006,** *45*, (21), 6953-6959.

710 44. Deen, W. M., Hindered Transport of Large Molecules in Liquid-Filled Pores.
711 *AIChE J.* **1987,** *33*, (9), 1409-1425.

712 45. Richards, L. A.; Richards, B. S.; Corry, B.; Schäfer, A. I., Experimental Energy
713 Barriers to Anions Transporting through Nanofiltration Membranes. *Environ. Sci.*
714 *Technol.* **2013,** *47*, (4), 1968-1976.

715 46. Sigurdardottir, S. B.; DuChanois, R. M.; Epsztein, R.; Pinelo, M.; Elimelech, M.,
716 Energy Barriers to Anion Transport in Nanofiltration Membranes: Role of Intra-Pore
717 Diffusion. *J. Membr. Sci.* **2020,** *603*, 117921.

718 47. Tunuguntla, R. H.; Henley, R. Y.; Yao, Y.-C.; Pham, T. A.; Wanunu, M.; Noy, A.,
719 Enhanced Water Permeability and Tunable Ion Selectivity in Subnanometer Carbon
720 Nanotube Porins. *Science* **2017,** *357*, (6353), 792-796.

721 48. Zhou, X.; Wang, Z.; Epsztein, R.; Zhan, C.; Li, W.; Fortner, J. D.; Pham, T. A.;
722 Kim, J.-H.; Elimelech, M., Intrapore Energy Barriers Govern Ion Transport and
723 Selectivity of Desalination Membranes. *Sci. Adv.* **2020,** *6*, (48), eabd9045.

724 49. Sun, P.-F.; Kim, T.-S.; Kim, H.-S.; Ham, S.-Y.; Jang, Y.; Park, Y.-G.; Tang, C. Y.;
725 Park, H.-D., Improved Anti-biofouling Performance of Pressure Retarded Osmosis
726 (PRO) by Dosing with Chlorhexidine Gluconate. *Desalination* **2020,** *481*, 114376.

727 50. Ham, S.-Y.; Kim, H.-S.; Jang, Y.; Sun, P.-F.; Park, J.-H.; Lee, J. S.; Byun, Y.; Park,
728 H.-D., Control of Membrane Biofouling by 6-Gingerol Analogs: Quorum Sensing
729 Inhibition. *Fuel* **2019,** *250*, 79-87.

730 51. Kim, H.-S.; Ham, S.-Y.; Jang, Y.; Sun, P.-F.; Park, J.-H.; Hoon Lee, J.; Park,
731 H.-D., Linoleic Acid, A Plant Fatty Acid, Controls Membrane Biofouling via
732 Inhibition of Biofilm Formation. *Fuel* **2019,** *253*, 754-761.

733 52. Zhang, L.; Wang, H.; Yu, W.; Su, Z.; Chai, L.; Li, J.; Shi, Y., Facile and
734 Large-Scale Synthesis of Functional Poly(m-Phenylenediamine) Nanoparticles by
735 Cu^{2+}-assisted Method with Superior Ability for Dye Adsorption. *J. Mater. Chem.* **2012,**
736 *22*, (35), 18244.

737 53. Chai, L.; Wang, T.; Zhang, L.; Wang, H.; Yang, W.; Dai, S.; Meng, Y.; Li, X., A
738 Cu–m-Phenylenediamine Complex Induced Route to Fabricate
739 Poly(m-Phenylenediamine)/Reduced Graphene Oxide Hydrogel and Its Adsorption
740 Application. *Carbon* **2015,** *81*, 748-757.

741 54. Wang, L.; Song, X.; Wang, T.; Wang, S.; Wang, Z.; Gao, C., Fabrication and
742 Characterization of Polyethersulfone/Carbon Nanotubes (PES/CNTs) Based Mixed
743 Matrix Membranes (MMMs) for Nanofiltration Application. *Appl. Surf. Sci.* **2015,**
744 *330*, 118-125.

745 55. Yu, W.; Zhang, L.; Meng, Y.; Dai, S.; Su, Z.; Chai, L.; Wang, H., High
746 Conversion Synthesis of Functional Poly(m-Phenylenediamine) Nanoparticles by
747 Cu-OH-assisted Method and Its Superior Ability toward Ag^+ Adsorption. *Synth. Met.*
748 **2013,** *176*, 78-85.

749 56. Ma, L.; Qin, H.; Cheng, C.; Xia, Y.; He, C.; Nie, C.; Wang, L.; Zhao, C.,
750 Mussel-inspired Self-coating at Macro-interface with Improved Biocompatibility and
751 Bioactivity via Dopamine Grafted Heparin-like Polymers and Heparin. *J. Mater.*

Chem. B **2014,** *2*, (4), 363-375.

57. Zhang, X.; Jia, C.; Xue, Y.; Yang, P., Fabrication of RGO/g-C$_3$N$_4$ Composites via Electrostatic Assembly towards Charge Separation Control. *RSC Adv.* **2017,** *7*, (69), 43888-43893.

58. Bowen, W. R.; Mukhtar, H., Characterisation and Prediction of Separation Performance of Nanofiltration Membranes. *J. Membr. Sci.* **1996,** *112*, (2), 263-274.

59. Košutić, K.; Dolar, D.; Kunst, B., On Experimental Parameters Characterizing the Reverse Osmosis and Nanofiltration Membranes' Active Layer. *J. Membr. Sci.* **2006,** *282*, (1-2), 109-114.

60. Wadekar, S. S.; Vidic, R. D., Influence of Active Layer on Separation Potentials of Nanofiltration Membranes for Inorganic Ions. *Environ. Sci. Technol.* **2017,** *51*, (10), 5658-5665.

61. Liang, Y.; Zhu, Y.; Liu, C.; Lee, K.-R.; Hung, W.-S.; Wang, Z.; Li, Y.; Elimelech, M.; Jin, J.; Lin, S., Polyamide Nanofiltration Membrane with Highly Uniform Sub-Nanometre Pores for Sub-1 Å Precision Separation. *Nat. Commun.* **2020,** *11*, (1), 1-9.

62. Van der Bruggen, B.; Vandecasteele, C., Modelling of the Retention of Uncharged Molecules with Nanofiltration. *Water Res.* **2002,** *36*, (5), 1360-1368.

63. Yang, G.; Shi, H.; Liu, W. Q.; Xing, W. H.; Xu, N. P., Investigation of Mg^{2+}/Li$^+$ Separation by Nanofiltration. *Chinese J Chem Eng* **2011,** *19*, (4), 586-591.

64. Ben-Sasson, M.; Zodrow, K. R.; Genggeng, Q.; Kang, Y.; Giannelis, E. P.; Elimelech, M., Surface Functionalization of Thin-Film Composite Membranes with Copper Nanoparticles for Antimicrobial Surface Properties. *Environ. Sci. Technol.* **2014,** *48*, (1), 384-393.

65. Kochkodan, V.; Hilal, N., A Comprehensive Review on Surface Modified Polymer Membranes for Biofouling Mitigation. *Desalination* **2015,** *356*, 187-207.

1

<u>Supporting Information</u>

A novel positively-charged metal-coordinated

nanofiltration membrane for lithium recovery

Li Wang[a,b], Danyal Rehman[c], Peng-Fei Sun[d], Akshay Deshmukh[c], Liyuan Zhang[b], Qi

Han[a], Zhe Yang[b*], Zhongying Wang[a*], Hee-Deung Park[d], John H. Lienhard[c*] and

Chuyang Y. Tang[b]

[a] School of Environmental Science and Engineering, Southern University of Science
and Technology, Shenzhen 518055, China
[b] Department of Civil Engineering, the University of Hong Kong, Pokfulam, Hong
Kong, SAR, P. R. China
[c] Department of Mechanical Engineering, Massachusetts Institute of Technology,
Cambridge MA 02139, USA
[d] School of Civil, Environmental and Architectural Engineering, Korea University,
Seoul, 02841, South Korea

[*] to whom correspondence should be addressed.

Zhongying Wang   e-mail: wangzy6@sustech.edu.cn;   tel.: +86-075588018040;

Zhe Yang   e-mail: zheyang@connect.hku.hk;   tel.: +852-2857 8470;

John H. Lienhard   e-mail: lienhard@mit.edu.;   tel.: +1-617-253-3790

23

Contents

24

Figure S1. (a) SEM images of prepared membranes, (b) digital photos of prepared Cu-MPD membranes. (c) the cross-section SEM image of membrane Cu1/2-MPD.
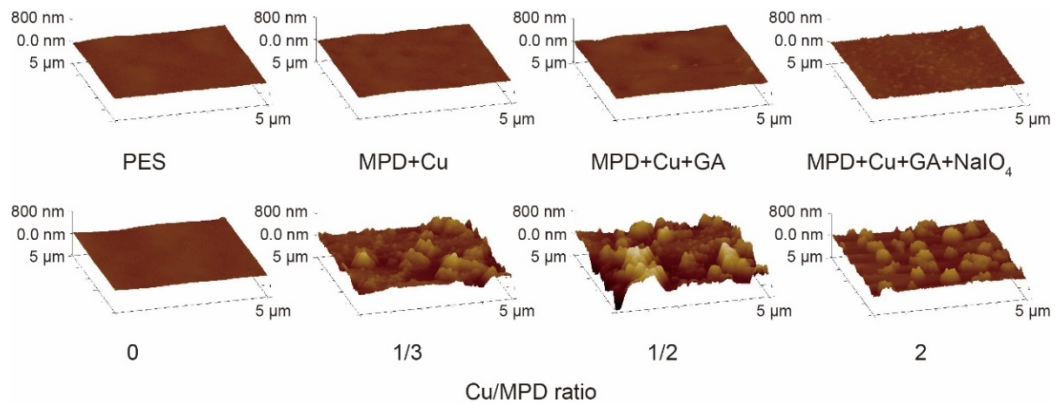
29
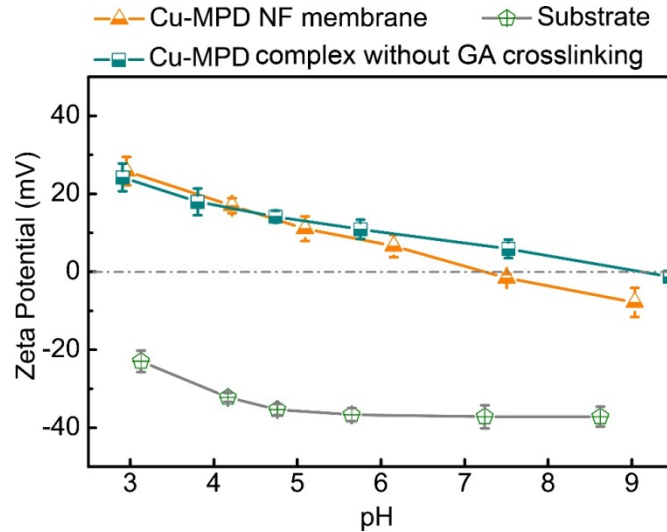
Figure S2. Zeta potential measurements of Cu-MPD NF membrane, Cu-MPD complex without GA crosslinking and PES substrate as a function of pH.

32

**Figure S3.** AFM images of prepared membranes with different compositions and different Cu/MPD ratios.

36

The amino groups in the Cu-MPD membrane contributes greatly in the positive-charge property of the membrane while the copper also plays an important role. Zeta potential of the Cu-MPD series membranes was measured at varied pH from 9 to 3. As shown in Figure S4., there was an obvious different between the trend of zeta potential for membrane Cu0-MPD and Cu1/2-MPD. We could conclude that below pH 5 the contribution of amino group dominated, while at pH higher than 5 the

43   effect of copper was significant. The two membranes also showed different

44   isoelectrical points. The isoelectrical point for Cu0-MPD was 5.3±0.3, and it was

45   7.4±0.2 for Cu1/2-MPD.
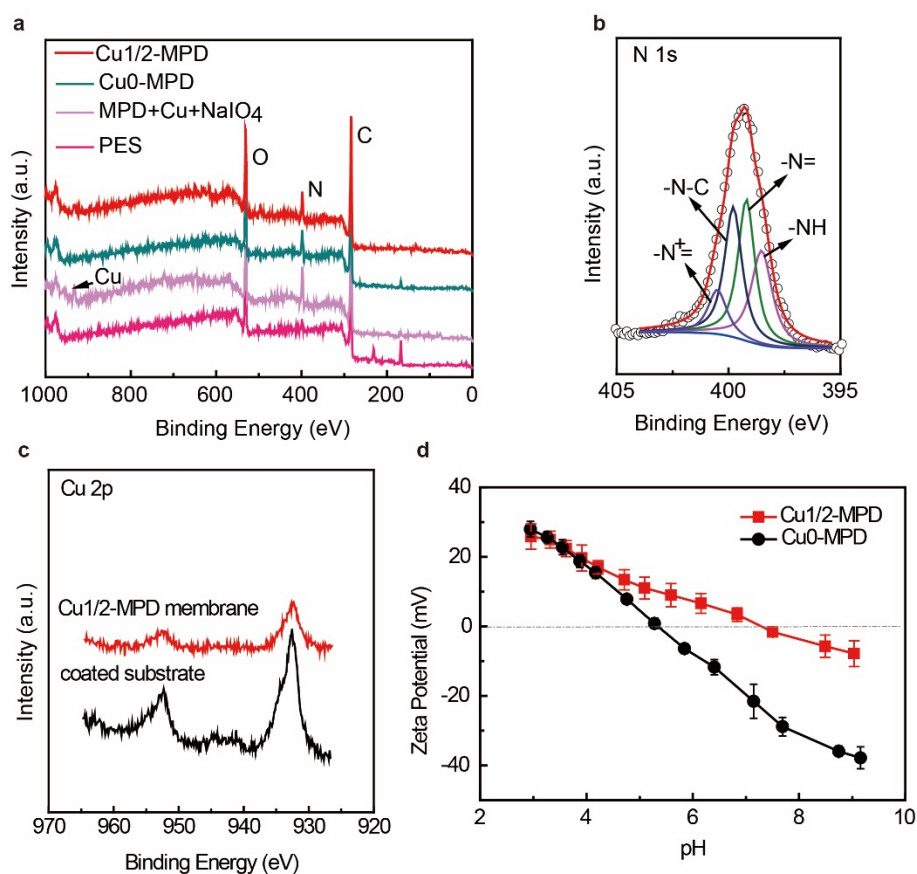
46
47   **Figure S4.** (a) XPS spectra of the prepared membranes. In Cu-MPD complex coated
48   sample, XPS spectra show peaks of Cu and enlarge N signals, but the S peak
49   belonging to PES substrate disappeared due to the surface coverage with Cu-MPD
50   complex. In Cu1/2-MPD, the peak of Cu could not be clearly seen, because of the low
51   mass of Cu and the cover of GA crosslinking. (b) N 1s spectrum of the Cu1/2-MPD
52   membrane, (c) the Cu 2p XPS spectra of both Cu-MPD coated substrate and
53   Cu1/2-MPD membrane. The existence of Cu in both the NF membrane Cu1/2-MPD
54   and coated substrate are confirmed, (d) zeta potential of Cu1/2-MPD and Cu0-MPD
55   membrane. A similar surface-positive-charge density has been showed in these two
56   membranes, indicating copper only plays a limit role in rejection at lower pH.
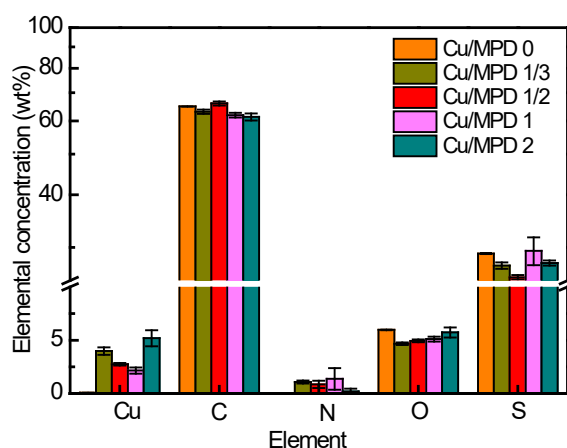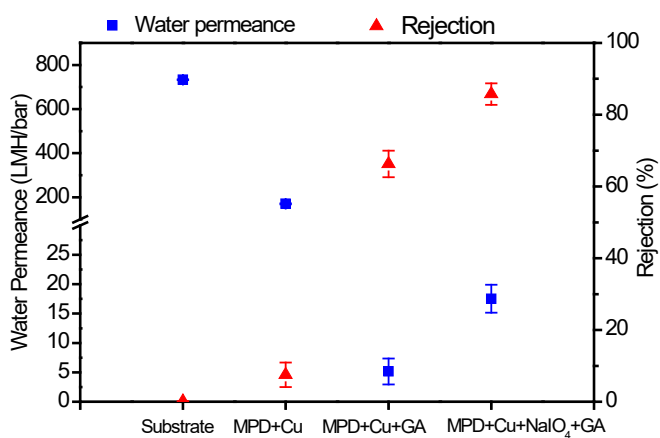
57

58 **Figure S5.** Copper loading in prepared membrane with different Cu/MPD ratios by
59 EDX.

60
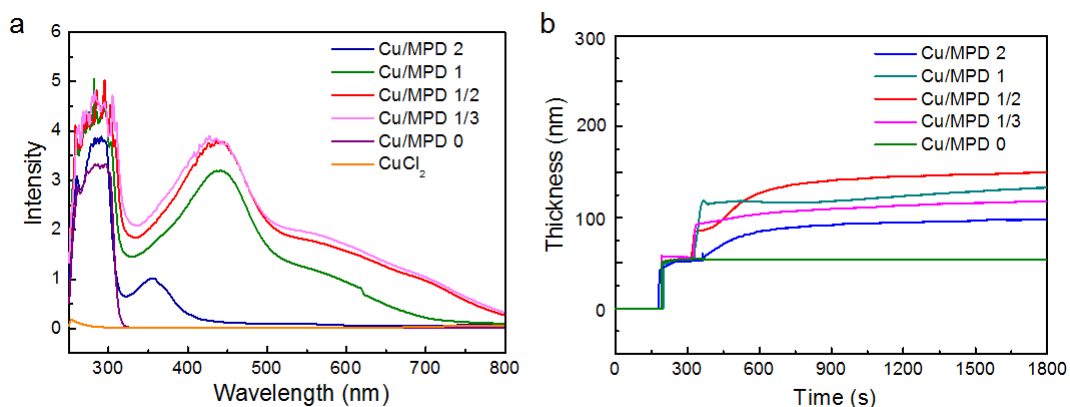
61

62 **Figure S6.** (a) UV-vis spectrum of Cu-MPD oligomers with different Cu/MPD ratios.
63 The reaction time was 30s. (b) Thickness of Cu-MPD oligomers with different
64 Cu/MPD ratios.

65

66 **Figure S7.** (a) Membrane separation performance. (a) pure water permeability and
67 rejection of the PES substrate, MPD+Cu, MPD+Cu+GA, MPD+Cu+NaIO$_4$+GA (Cu

68 membrane. All filtration tests are operated at 5 bar and the feed solution concentration
69 is 1000 ppm of $MgCl_2$, which are based on three replicate membrane coupons.
70

71 **Table S1.** The recipe for fabricating the Cu-MPD membrane.

Membrane type	Cu (wt%)	MPD (wt%)	NaIO$_4$ (wt%)	GA (wt%)
Substrate	0	0	0	0
MPD+Cu	1	1	0	0
MPD+Cu+GA	1	1	0	2
MPD+Cu +NaIO$_4$+GA	1	1	4	2

72

73 **Table S2.** Contact angle and isoelectrical point of prepared membranes.

Membrane type (Cu/MPD ratio)	Contact angle	Isoelectrical point
Substrate	56.9±1.7	< 3
0	37.5±4.6	5.3±0.3
1/3	40.2±2.5	7.3±0.2
1/2	54.1±4.0	7.4±0.2
1	16.2±2.0	7.0±0.2
2	23.9±1.3	5.2±0.3

74

75 **Table S3.** Comparison of this work to the literature.

Surface-charge	Membrane type	Feed concent-ration	Mg/Li mass ratio	pH	SF	Permeability	Li rejection	Pressure (pre-pressure time)	Reference
		ppm	ppm/ppm			LHM/bar	%	bar (h)	
Positive	Cu-MPD	2000	23.5	3	8.0	16.16	32.3	5(2)	This work
				5	6.7	13.76	30.2		
				6	6.1	11.36	21.2		
				7	4.9	10.36	22.2		
				9	3.9	9.05	21.7		
Positive	BPEI-TMC, coated with EDTA		24	5.5	9.2	0.6	~35*	10(2)	[1]
Positive	PEI-TMC	2000	20	6.5	20	5.02	19	8(0.5)	[2]

Charge	Membrane								Ref
Positive	PEI/MWCNT-TMC	2000	21.4	6.5	7.13	14.03	15	4(0.5)	3
Positive	DAPP-TMC	2000	20		2.6		-40.7*	3(0.5)	4
Negative	Janus NF membrane	2000	30		12.15	4.17	11.6	8(0.5)	5
			60		5.84	3.4	21.8	8(0.5)	
Negative	DK NF membrane (polyamide)		35.4	4	16	0.33		15(0.08)	6
Negative	NF 90	2000	20		2.1		15	3(0.5)	4
Negative	DL-2540		40		2.86		-10*		
Negative	Desal DK (GE Osmonics)	4940	18		3.13	17.36	-60*	16	
		3680	22		2.63	17.36	-30*	8	
		2500	24		2.63	27.78	-25*	10	7
Negative	DK-1812 model	6000	40		42	0.9	-170	8	

Table S4. Copper loading concentration.

Membrane type (Cu/MPD ratio)	Cu loading concentration $\mu g/cm^2$
0	ND
1/3	18.4±0.8
1/2	9.9±1.2
1	4.4±0.3
2	15.3±2.0

Membrane coupon with different components was immersed into 2% HNO_3 and shaken for 3 days, and then the Cu leaching concentration was measured by ICP-OES.
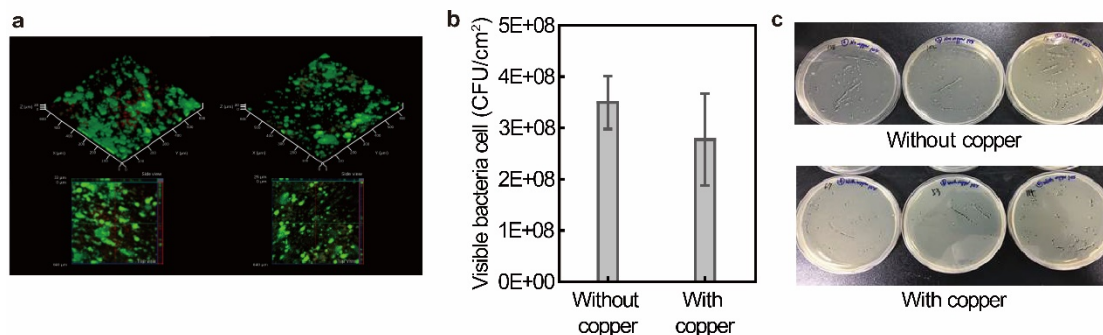
We also carried out the long-term running filtration to investigate the stability of the membrane. The testing result is presented in Figure S12. The Cu1/2-MPD membrane showed a maintained rejection in 72 h filtration, indicating its stability in long-term running application.
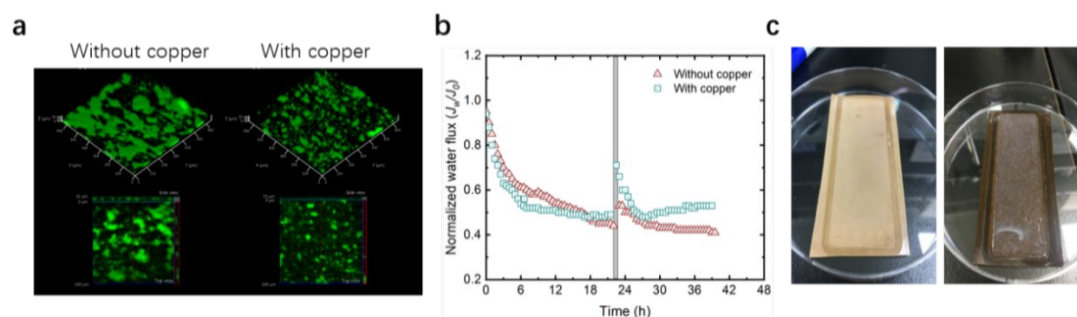
Figure S8. (a) the CLSM of membrane surface after the rotating disc filtration experiment, (b) bacteria cell number on the plates spread using the rinsing water from the membrane surface after rotating disc filtration with a P value of 0.03 and (c) digital photos of the spread plates in (b).

Figure S9. (a) the CLSM image of membrane surface with no copper and with Cu/MPD ratio of 1/2 after 40 h filtration at 5 bar; (b) normalized permeability of membrane with no copper and with Cu/MPD ratio of 1/2 in 40 h filtration at 5 bar; (c) the photos of membrane with no copper and with Cu/MPD ratio of 1/2 after 40 h filtration at 5 bar.
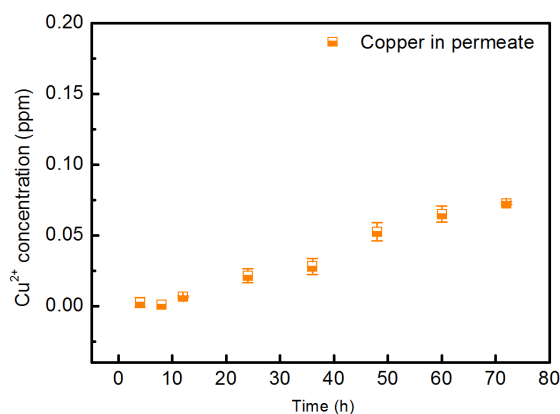
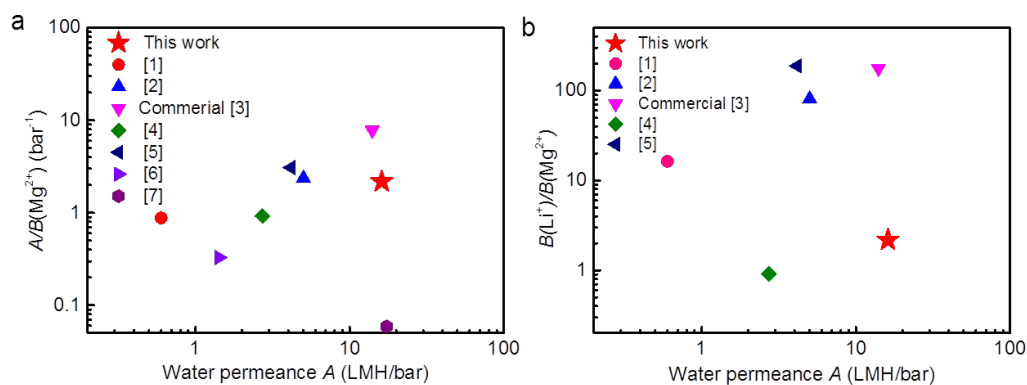**Figure S10.** Copper leaching test in pure water through a dynamic cross-flow filtration for the Cu1/2-MPD membrane at pH 7 with an applied pressure of 5 bar.

104

105 **Figure S11.** (a) Tradeoff between membrane water permeance (A) and membrane
106 water/MgCl$_2$ selectivity (A/B) and (b) Tradeoff between water permeance and
107 B_{Li+}/B_{Mg2+} ratio based on the literature survey of NF membranes and some
108 commercial NF membranes in Table S3. B value can be calculated by $J_w(1-R)/R$.

109

110   To evaluate the effect of Na$^+$ on the membrane performance, we have tested

111 membrane performance with the presence of Na$^+$. Specifically, the mass of the added

112 Na$^+$ was equal to the amount that was needed to adjust pH from 7 to 9 (we did not add

113 NaOH for brine with pH lower than 7; instead, we adjusted the pH with HCl). The

114 results show that presence of Na$^+$ didn't show any effect on the membrane

115 performance in the 72 h filtration.

116

117

118
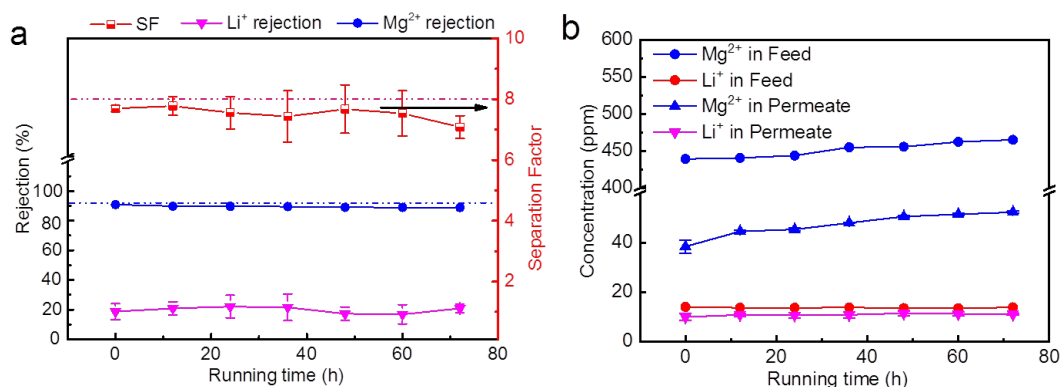
119 **Figure S12.** Membrane long-term running stability test for 72 h, pH 3, at an applied
120 pressure of 5 bar. (a) SF, Li$^+$ and Mg^{2+} rejection at the presence of Na$^+$ with
121 equivalent molar amount of NaCl to that of NaOH used adjusting from pH 7 to 9. The

dash line represents the corresponding control membrane without the addition of
123 NaCl and (b) the concentration of Li^+ and Mg^{2+} in permeate and feed.
124
125

126
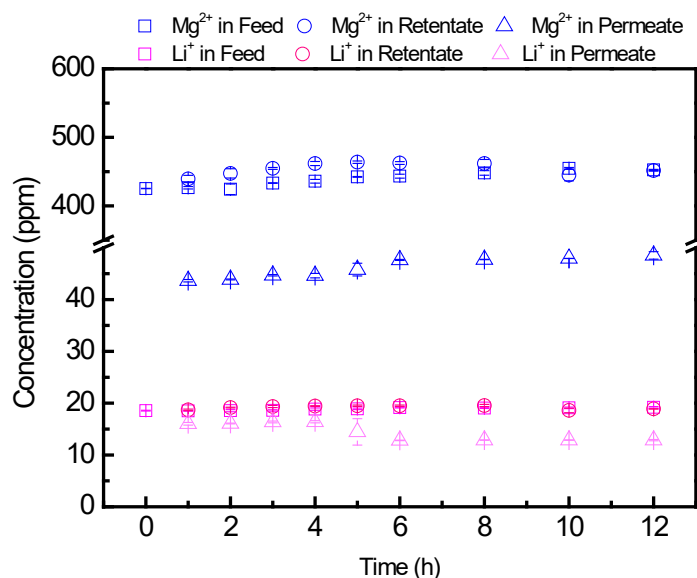
Figure S13. Membrane separation performances tests by measuring the concentration
128 of Li^+ and Mg^{2+} feed, retentate and permeate solution at an applied pressure of 5 bar
129 for Cu1/2-MPD NF membrane at pH3.

130

131

Table S5. Average biofilm thickness and average biovolume on surface of membrane
133 with no copper and with Cu/MPD ratio of 1/2.

Membrane	Average biofilm thickness (μm)		Average biovolume (μm³/μm²)	
	Live cell	Dead cell	Live cell	Dead cell
No copper[1]	9.3±1.9	21.7±5.1	5.7±2.2	10.5±1.5
With copper[1]	1.9±1.5	0.5±0.4	1.3±0.9	0.2±0.1
No copper[2]	48.5±6.8	61.6±3.1	36.9±5.3	51.0±2.7
With copper[2]	36.1±8.2	43.3±14.8	21.9±5.5	29.5±15.6
No copper[3]	7.4±2.7	27.8±8.1	5.6±1.6	16.8±6.0
With copper[3]	9.8±5.1	18.3±5.7	7.4±4.1	14.1±4.9

Note

135 [1] membrane after 10 h filtration at 10 bar;
136 [2] membrane after 40 h filtration at 5 bar.
137 [3] membrane after rotating disc filtration.

138

139 The ICP samples have been filtrated by 0.22 μm PES filter in order not to

140 contaminate the ICP. Therefore, I and Cu, that facilitate the formation of the Cu-MPD

141 complexes, may also be filtered out within its large-sized aggregates. Considering that

142 it is beyond the current scope of this work, we decide not to over-interpret these

143 results. However, future studies could address this issue through advanced

144 characterization techniques.

145

146 **Table S6.** I and Cu concentration before and after 5h reaction. All samples have been
147 diluted for 1000 times.

Sample	I (ppm)	Cu (ppm)
0h	3.28±0.26	2.28±0.02
5h	3.06±0.03	2.44±0.03

148

149

150 **Table S7**. Performance of membrane with different recipes.

Membrane Type	Permeability (LMH/bar)	$MgCl_2$ Rejection (%)
Cu0-MPD-GA	1.9 ± 0.1	22.5 ± 2.4
Cu1/2-MPD-GA	10.6 ± 0.7	90.0 ± 1.2
Cu0-MPD-GA0	96.6 ± 6.6	6.5 ± 1.7
Cu1/2-MPD-GA0	53.3 ± 4.1	54.8 ± 4.6

151 Notes: GA0 and Cu0 mean no GA or Cu was incorporated during the polymerization
152 process.

153

154 **Table S8**. The recipe of the membranes in Table S7.

Membrane type	Cu (wt%)	MPD (wt%)	$NaIO_4$ (wt%)	GA(wt%)
Cu0-MPD-GA	0	2	4	2
Cu1/2-MPD-GA	1	2	4	2
Cu0-MPD-GA0	0	2	4	0
Cu1/2-MPD-GA0	1	2	4	0

155

156

157

158

159   **References:**

160   1.   Li, W.; Shi, C.; Zhou, A.; He, X.; Sun, Y.; Zhang, J., A Positively Charged
161   Composite Nanofiltration Membrane Modified by EDTA for LiCl/MgCl$_2$ Separation.
162   *Sep. Purif. Technol.* **2017,** *186*, 233-242.
163   2.   Xu, P.; Wang, W.; Qian, X.; Wang, H.; Guo, C.; Li, N.; Xu, Z.; Teng, K.; Wang,
164   Z., Positive Charged PEI-TMC Composite Nanofiltration Membrane for Separation of
165   Li$^+$ and Mg^{2+} from Brine with High Mg^{2+}/Li$^+$ Ratio. *Desalination* **2019,** *449*, 57-68.
166   3.   Zhang, H.-Z.; Xu, Z.-L.; Ding, H.; Tang, Y.-J., Positively Charged Capillary
167   Nanofiltration Membrane with High Rejection for Mg^{2+} and Ca^{2+} and Good
168   Separation for Mg^{2+} and Li$^+$. *Desalination* **2017,** *420*, 158-166.
169   4.   Li, X.; Zhang, C.; Zhang, S.; Li, J.; He, B.; Cui, Z., Preparation and
170   Characterization of Positively Charged Polyamide Composite Nanofiltration Hollow
171   Fiber Membrane for Lithium and Magnesium Separation. *Desalination* **2015,** *369*,
172   26-36.
173   5.   Guo, C. S.; Li, N.; Qian, X. M.; Shi, J.; Jing, M. L.; Teng, K. Y.; Xu, Z. W.,
174   Ultra-Thin Double Janus Nanofiltration Membrane for Separation of Li$^+$ and Mg^{2+}:
175   "Drag" Effect from Carboxyl-containing Negative Interlayer. *Sep. Purif. Technol.*
176   **2020,** *230*, 115567.
177   6.   Li, Y.; Zhao, Y.; Wang, H.; Wang, M., The Application of Nanofiltration
178   Membrane for Recovering Lithium from Salt Lake Brine. *Desalination* **2019,** *468*.
179   7.   Yang, G.; Shi, H.; Liu, W. Q.; Xing, W. H.; Xu, N. P., Investigation of Mg^{2+}/Li$^+$
180   Separation by Nanofiltration. *Chinese J Chem Eng* **2011,** *19*, (4), 586-591.

181